Zero-Index Weyl Metamaterials

Farzad Zangeneh-Nejad and Romain Fleury*
Laboratory of Wave Engineering, Swiss Federal Institute of Technology in Lausanne (EPFL), 1015 Lausanne, Switzerland

(Received 14 February 2020; accepted 9 July 2020; published 28 July 2020)

Depending on the geometry of their Fermi surfaces, Weyl semimetals and their analogs in classical systems have been classified into two types. In type-I Weyl semimetals (WSMs), the conelike spectrum at the Weyl point is not tilted, leading to a pointlike closed Fermi surface. In type-II WSMs, on the contrary, the energy spectrum around the Weyl point is strongly tilted such that the Fermi surface transforms from a point into an open surface. Here, we demonstrate, both theoretically and experimentally, a new type of (classical) Weyl semimetal whose Fermi surface is neither a point nor a surface, but a flat line. The distinctive Fermi surfaces of such semimetals, dubbed as type-III or zero-index WSMs, gives rise to unique physical properties: one of the edge modes of the semimetal exhibits a zero index of refraction along a specific direction, in stark contrast to type-I and type-II WSMs for which the index of refraction is always nonzero. We show that the zero-index response of such topological phases enables exciting applications such as extraordinary wave transmission.

DOI: 10.1103/PhysRevLett.125.054301

Weyl semimetals (WSMs) have recently attracted enormous research interest because of their unconventional band structures and topological features [1–4]. In the Brillouin zone of a WSM, the valence and conduction bands touch each other at a set of points, called Weyl points (WPs) [5–11]. These points are sources and drains of Berry curvature in the momentum space and, thus, can be associated with a topological charge [12]. The topological nature of WPs protects them against annihilation in case of small perturbations, and leads to a large variety of intriguing physical phenomena such as superconductivity [13,14], chiral anomaly [14,15], and topological negative refraction [16].

Although it is not possible to remove Weyl nodes because of their topological character, the energy dispersion at a WP might, in principle, be tilted along a certain direction. While such a tilting of the band structure does not affect the essential topology of the WP, it can change the bulk properties of the semimetallic phase by modifying the geometry of the Fermi surface [17]. As such, depending on whether their conelike band structure is tilted or not, WSMs and their classical analogs have been grouped into two types. In a standard (type-I) WSM [18,19], the energy dispersion at the WP is not tilted, leading to a pointlike Fermi surface. In type-II WSMs [20–27], on the other hand, the energy spectrum around the Weyl node is strongly tilted (by an angle larger than a specific angle θ_c, at which parts of the conduction and valence bands start to coexist in energy). As a result, the conelike dispersion around the WP tips over and the Fermi surface transforms from a single point into an open surface. This gives rise to distinctive physical properties for type-II WSMs such as orientation dependent chiral anomaly and anomalous Hall effects [28,29].

So far, Weyl semimetals have been studied when the tilting angle at the WP is both smaller than θ_c (type-I WSMs) and larger than θ_c (type-II WSMs). Here, on the contrary, we investigate in theory, simulation, and experiment the exotic properties of classical Weyl semimetals when their energy spectrum is tilted exactly by θ_c. We show that the Fermi surface of such kinds of semimetallic phases is neither a point, as in type-I WSMs, nor a surface, as in type-II WSMs. Instead, it is a line connecting a pair of WPs. Since the geometry of the Fermi surface plays a very important role in determining the bulk properties of WSMs, we categorize these new kinds of semimetals into a distinct group, referred to as type-III or "zero-index" WSMs. Such an appellation is inspired by the fact that, as opposed to type-I and type-II WSMs possessing a nonzero index of refraction in all directions, the topological surface states of the proposed WSM exhibit a zero group velocity, or more precisely, a zero-index response along a specific direction. This behavior generalizes to three dimensions the zero-index response of the edge modes of type-III Dirac semimetals [22]. We demonstrate that the staticlike behavior of type-III Weyl semimetals can be used to achieve extraordinary wave transmission, akin to anomalous tunneling in the so-called zero-index metamaterials [30–33].

To start, we consider the tight-binding crystal shown in Fig. 1(a), described by the tight-binding Hamiltonian,

$$H = 2\lambda_z \cos k_z \sigma_0 + (2\lambda_x \cos k_x + 2\lambda_y \cos k_y)\sigma_x + 2\delta_x \sin k_x \sigma_y + 2\delta_z \cos k_z \sigma_z, \quad (1)$$

in which σ_0, $\sigma_{x,y,z}$ are identity and Pauli matrices, respectively, and k_x, k_y, and k_z are the Bloch wave numbers. We

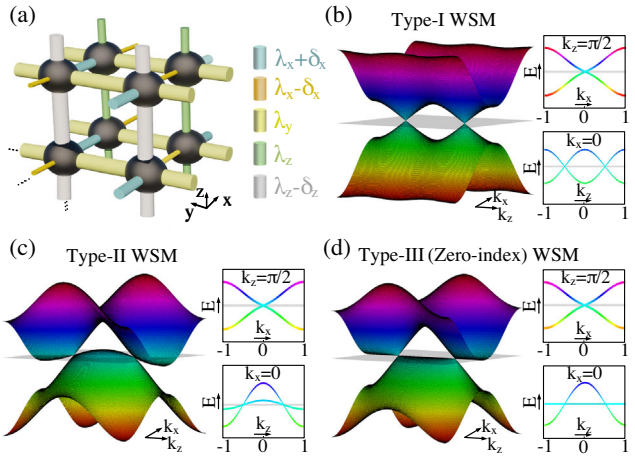

FIG. 1. Zero-index (type-III) Weyl semimetals. (a) We consider a tight-binding model consisting of a set of resonators coupled to each other with specified hopping strengths. (b) Band structure of the crystal for $\lambda_x = 1$, $\lambda_y = 2$, $\lambda_z = 2$, $\delta_x = 0.5$, and $\delta_z = 0$, calculated at the plane $k_y = 2\pi/3$. The band structure supports a pair of gap-closing Weyl points (WPs). The conical dispersion around the WP is not tilted, leading to a pointlike Fermi surface (type-I WSM). (c) Same as (b) except that the parameter δ_z is chosen to be $\delta_z = 2\lambda_z$. The energy spectrum at the WP is strongly tilted in this case, so that the Fermi surface transforms from a point into an open surface (type-II WSM). (d) Same as (b) and (c) but for $\delta_z = \lambda_z$. In this case, the canonical spectrum around the WP is tilted by the critical angle θ_c, at which the valence and conduction bands start to coexist in energy. The Fermi surface of the corresponding semimetallic phase is neither a point nor a surface, but is a completely flat line. This gives rise to a zero-index response for the semimetal.

assume $\lambda_x = 1$, $\lambda_y = 2$, $\lambda_z = 2$, and $\delta_x = 0.5$. Furthermore, for now, we suppose that the parameter δ_z is set to be zero; i.e., $\delta_z = 0$. With these choices of parameters, the tight-binding Hamiltonian H vanishes at P: $(k_x, k_y, k_z) = (0, \pm 2\pi/3, \pm\pi/2)$, implying that the dispersion bands of the two-level system cross each other at these four points. As an example, we report in Fig. 1(b) the energy band structure of the corresponding Hamiltonian at the plane $k_y = 2\pi/3$, which includes two of these crossing points at $(k_x, k_z) = (0, \pm\pi/2)$. These crossing points are Weyl nodes, possessing opposite chiralities (see Ref. [34]). The energy dispersion around these Weyl nodes is not tilted, leading to a pointlike closed Fermi surface (characteristic of type-I WSMs).

Next, suppose that the parameter δ_z is set to be $\delta_z = 2\lambda_z$. The corresponding band structure at the plane $k_y = 2\pi/3$ is shown in Fig. 1(c). Like the previous case, the band structure exhibits a pair of Weyl points located at $(k_x, k_z) = (0, \pm\pi/2)$. However, as opposed to the previous case, the cone-spectrum is significantly tilted around these nodes, so that some modes from the valence band coexist in energy with others in the conduction band. Such a strong tilting modifies the geometry of the Fermi surface: it becomes an open surface (characteristic of type-II WSMs [20]).

Now we assume $\delta_z = \lambda_z$. Figure 1(d) represents the corresponding band structure at $k_y = 2\pi/3$. Similar to the previous two cases, the band structure exhibits two Weyl nodes at $(k_x, k_z) = (0, \pm\pi/2)$. Around these points, the energy band structure is tilted, similar to what we had in the latter case. However, the tilting angle is exactly equal to the critical angle θ_c, leading to a Fermi surface which is neither a single point, like type-I WSMs, nor an open surface, like type-II WSMs, but a straight line connecting a pair of Weyl points [34]. Such a unique Fermi surface gives rise to unique physical properties for the semimetallic phase (referred to as type-III WSM), as demonstrated below.

We first investigate the topological boundary states carried by zero-index Weyl semimetals. To this end, we consider a $100 \times 1 \times 1$ supercell of the crystal and calculate the corresponding dispersion surfaces [34]. The resulting band structure is represented in Fig. 2(a), clearly showing the existence of two helical gap-closing topological edge states. In order to further analyze this result, we report the dispersion curves corresponding to three different plane sections, namely, $k_y = \pi$, $k_y = 2\pi/3$, and $k_y = 0$ [Figs. 2(b)–2(d), respectively]. As explained earlier, the plane $k_y = 2\pi/3$ is the one at which the Weyl transition occurs, so the band structure is gapless at this plane [Fig. 2(c)]. As confirmed by direct calculations, the constant-k_y planes before ($k_y = 0$)

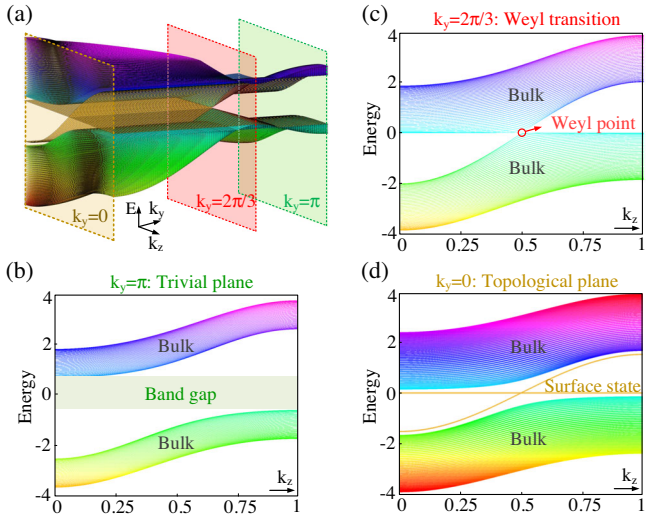

FIG. 2. Topological boundary states of the proposed zero-index WSM. (a) Dispersion surfaces of the $100 \times 1 \times 1$ supercell of the zero-index WSM. The band structure supports two helical topological boundary states (yellow surfaces). (b) Band structure of the supercell at $k_y = \pi$, which is completely gapped because the plane section has a zero topological invariant. (c) Same as (b) but for the plane $k_y = 2\pi/3$. The band structure is gapless at this plane. (d) Same as (b) and (c) except that the band structure is calculated at the plane $k_y = 0$, corresponding to a nonvanishing topological invariant. The band structure exhibits gap-closing topological boundary states. Importantly, one of these boundary states possesses a completely flat dispersion, i.e., a zero group velocity along z.

and after ($k_y = \pi$) this critical point possess different $\mathbb{Z}_2$ topological invariants, making the system a $\mathbb{Z}_2$ Weyl semimetal [34]. In particular, $k_y = \pi$ has a zero invariant [34], consistent with the fully gapped dispersion diagram of Fig. 2(b). Conversely, $k_y = 0$ is associated with a nonvanishing invariant [34], explaining the two helical topological surface states observed in Fig. 2(d). Remarkably, in contrast to type-I and type-II WSMs for which the gapless states have always a nonzero group velocity, one of the associated helical topological surface states of the obtained WSM has a zero group velocity along k_z (note that in directions other than k_z, the edge mode remains dispersive). The origin of this behavior is linked to the balance between the σ_0 and σ_z terms in Eq. (1), canceling one of the diagonal elements of the Hamiltonian at the critical angle.

Next, we investigate an implementation of the proposed zero-index WSM using the sonic crystal shown in Fig. 3(a), consisting of Helmholtz resonators connected to each other via acoustic channels with varying widths (see Ref. [34] for a geometrical description). Full-wave simulations [34] confirm that the band structure of the crystal displays a type-III Weyl semimetallic phase [Fig. 3(b)]. Figure 3(c) represents the band structure of a $11 \times 1 \times 1$ supercell of the crystal. Consistent with our prior findings, the band

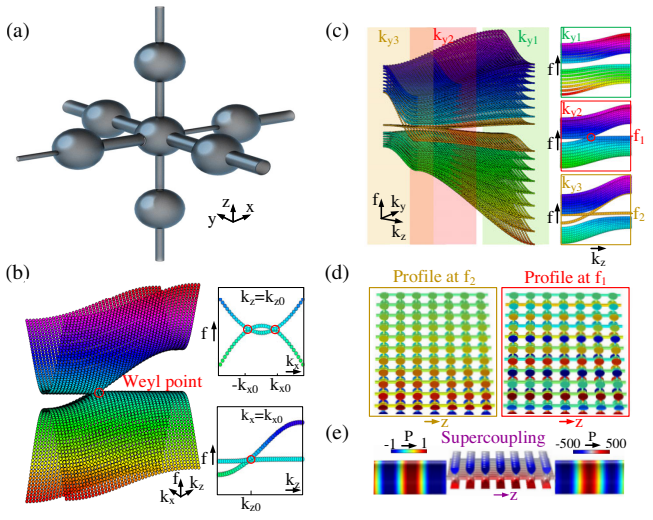

FIG. 3. Topological acoustic supercoupling induced by zero-index WSMs. (a) We consider a three-dimensional sonic crystal, with Helmholtz resonators connected to each other via acoustic channels with specific widths, realizing a zero-index acoustic WSM. (b) Band structure of the infinite sonic crystal, resembling the band structure of the type-III WSM described before. (c) Dispersion surfaces of a supercell of the crystal. Similar to our previous observations, the obtained band structure consists of plane sections with different topological properties. (d) Left: Mode profile of the crystal at the frequency f_2. The edge mode has a staticlike distribution along the z axis. Right: Pressure distribution at the frequency f_1. The bulk mode is also uniform along z. (e) Demonstration of extraordinary transmission of sound through the zero-index topological boundary state.

structure of the supercell consists of plane sections with different topologies. At the topological plane ($k_y = k_{y3}$), the crystal supports two helical surface states, one of which has a near-zero index of refraction along z (note that, due to longer-range hopping, the associated effective index is not exactly zero, but near it). To obtain more insight into the physics of the near-zero-index topological edge mode, we plot in Fig. 3(d) (left-hand panel) the associated acoustic pressure field, obtained via eigenfrequency simulations [34]. It is seen that, along the z direction, this mode has a quasistatic pressure distribution. This is equivalent to an infinite phase velocity along the edge of the semimetal. Interestingly, such a zero-index behavior also occurs at another cut plane of the band structure, namely the transition plane $k_y = k_{y2}$. This is demonstrated in Fig. 3(d) (right), reporting the associated acoustic field profile at this plane for $k_z = 0$.

The staticlike behavior of type-III (zero-index) topological phases enables exciting physical phenomena. Figure 3(e), for example, demonstrates the possibility of achieving extraordinary transmission of sound [40] by direct anomalous matching of an external waveguide to the near-zero topological edge mode of the 2D topological cut plane of the Weyl semimetal. Because of the small value of both the effective density and bulk modulus of the edge channel, the edge mode is impedance matched to the external waveguides (when neglecting losses, see Ref. [34]), leading to the transmission amplitude of near unity (0.988) with almost no phase lag (0.052 rad). Note that, markedly different from Fabry-Perot resonances, the obtained anomalous resonance tunneling does not depend on the length of the semimetallic connection [33,34].

Now, we experimentally investigate such anomalous tunneling through the edge mode at a topological cut plane, based on the fabricated prototype of the sonic crystal shown in Figs. 4(a) and 4(b). Note that, as explained in Ref. [34], picking this particular 2D cut plane allows building only one layer of the 3D system. This one-layer system may also be viewed as a type-III Dirac semimetal [22], supporting a 1D zero-index topological edge mode. Two external waveguides are connected to the edge of the fabricated prototype, with a loudspeaker at the entrance of the first and an anechoic termination in the second. Four microphones probe the acoustic pressure distribution along the edge of the semimetal. Full-wave simulations (neglecting losses) predict zero-index tunneling of sound through the edge at the frequency $f_0 = 2.92$ kHz. In practice, due to the presence of absorption, the transmission coefficient of the fabricated structure does not reach unity at this frequency. However, the existence of the edge mode at f_0 and its staticlike phase profile are not affected by the losses, and can be probed in experiment [34]. Figure 4(c) (top) reports the sound pressure level spectrum measured by microphone number 3. Near f_0, a resonance peak is observed, corresponding to the near-zero topological edge

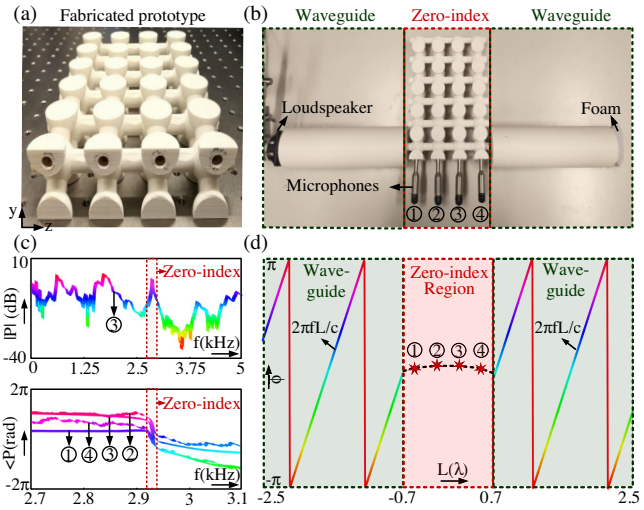

FIG. 4. Experimental demonstration of anomalous tunneling through the topological zero-index edge mode. (a) Fabricated prototype of a zero-index semimetal. (b) Experimental setup used to verify the anomalous tunneling through the zero-index topological edge mode. (c) (Top) Spectrum of the sound pressure level inside the zero-index crystal, measured by the microphone 3. The spectrum exhibits a resonance peak at the frequency of $f_0 = 2920$ Hz, corresponding to the near-zero index anomalous tunneling. (Bottom) Variation of the pressure phases, measured by each of the four microphones, as a function of frequency. Around f_0, the four measured spectra are almost identical, indicating the zero-index character of the crystal within this frequency range. (d) Variation of the pressure phase along the edge of the crystal (red region) compared to the phase variation in external waveguides ($\varphi = 2\pi f L/c$).

mode. The quasistatic nature of the edge mode is confirmed in Fig. 4(c) (bottom), reporting the phases of the pressure field at all four microphones versus frequency. As observed, near f_0, the corresponding phase spectra converge to almost the same value. To further illustrate the near-zero-index response of the topological edge mode, we report in Fig. 4(d) the variation of the pressure phase at f_0 along the edge of the crystal (red region), together with the standard phase variation in waveguides, i.e., $\varphi = 2\pi f_0 L/c$ (green region). This figure confirms the quasistatic sound propagation along the edge of the semimetal with almost no phase variations along a distance of 1.4 acoustic wavelengths.

Finally, leveraging the concept of synthetic dimensions [41–44], we measure the complete band structure of the type-III Weyl semimetal. To this end, we consider a one-dimensional sonic crystal made from evanescently coupled acoustic bound states in continuum [45–49] with on-site frequencies ω_n and hopping rates k_n following the equations $\omega_n = 2\lambda_z \cos\varphi_z[1 + (-1)^n]$ and $k_n = \lambda_x + (-1)^n\delta_x + \lambda_y \cos\varphi_y$ [34]. It is straightforward to verify that, upon replacing φ_y with k_y and φ_z with k_z, the tight-binding Hamiltonian of this one-dimensional chain is identical to Eq. (1). Therefore, the complete semimetallic band structure can be probed considering the family of one-dimensional sonic systems generated when sweeping the parameters φ_y and φ_z in a synthetic 3D Brillouin zone. We report in Figs. 5(a)–5(c) the band structures of the chains versus k_z (φ_z) at three different k_y (φ_y), namely, $k_y = \pi$, $k_y = 2\pi/3$, and $k_y = 0$, respectively, obtained by full-wave eigenfrequency simulations. Consistent with our previous tight-binding studies, at $k_y = \pi$, the energy spectrum is gapped. Contrarily, at $k_y = 2\pi/3$, it is gapless and exhibits a pair of Weyl points, connected to each other with a flat line. At $k_y = 0$, which is a plane with a nonzero $\mathbb{Z}_2$ charge, the two gap-closing helical surface states are indeed found, one of them with a zero group velocity.

To extract the band structure of the crystal from far-field scattering tests, we excite the system under study with a plane wave and measure the corresponding transmission spectra by performing standard standing-wave pattern analysis [34]. The evolution of the transmission coefficient of the structure as a function of both frequency and k_z is plotted in Figs. 5(d)–5(f), corresponding respectively to $k_y = 0$ [Fig. 5(d)], $k_y = 2\pi/3$ [Fig. 5(e)], and $k_y = \pi$ [Fig. 5(f)]. It is observed that the distinctive characteristics of the band structure of the crystal, including the peculiar dispersion of the topological edge modes [Figs. 5(a)–5(c)],

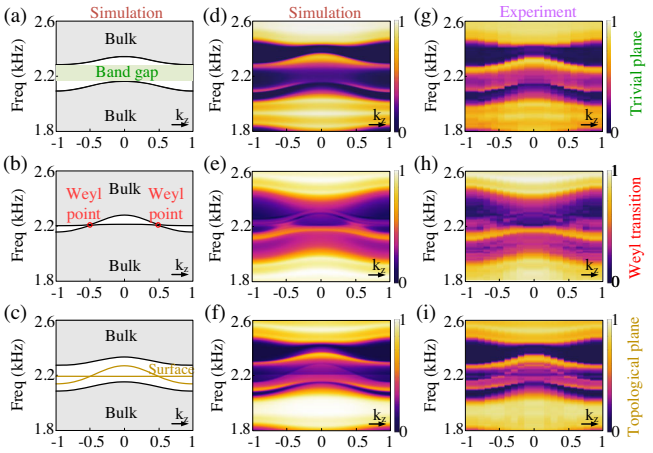

FIG. 5. Experimental observation of zero-index Weyl semimetals. We map the tight-binding model represented in Fig. 1 into a one-dimensional phononic crystal [34] with two additional phason degrees of freedom, φ_y and φ_z, taking the role of synthetic Bloch wave numbers (k_y and k_z). (a) Eigenfrequency spectrum of the sonic crystal at the plane $k_y = 0$, possessing a zero topological index. (b) Same as (a) but for $k_y = 2\pi/3$ (the plane on transition). (c) Same as (a) and (b) except that we set $k_y = \pi$. The band structure exhibits a zero-index topological boundary state. (d)–(f) Resolution of the obtained eigenfrequency spectra based on the corresponding transmission spectra plotted as a function of frequency and k_z, for $k_y = 0$ (d), $k_y = 2\pi/3$ (e), and $k_y = \pi$ (f). (g)–(i) Corresponding experimental measurements, showing good agreement with simulations.

translate into clear features in the scattering spectrum [Figs. 5(d)–5(f)], namely transmission maxima or minima.

These findings are verified in experiment, based on one-dimensional sonic crystals of plastic rods arranged inside an acoustic waveguide [34]. By changing the radii of the rods and the distance between them, the on-site frequencies and hopping rates of the 1D bound states in continuum chain were tuned according to the prescribed relations, so as to resolve the dispersion bands of the proposed semimetal. The results of our experiment, shown in Figs. 5(g)–5(i), agree well with simulation.

To conclude, we explored the properties of zero-index WSMs and demonstrated their intriguing dispersion properties in theory, simulation, and experiment. The unconventional character of the topological boundary states of zero-index WSM may open exciting venues for a large variety of engineering-oriented applications, for example, energy concentration, supercoupling, wave front shaping, and subwavelength imaging. Future studies may investigate non-Hermitian effects that could arise in the strong absorption regime, such as the creation of exceptional rings and their effect on the edge states. This may be experimentally reached by designing geometries supporting larger viscothermal losses [35–37].

This work was supported by the Swiss National Science Foundation (SNSF) under Grant No. 172487.

*Corresponding author.
romain.fleury@epfl.ch

[1] H. Weyl, Elektron und gravitation. I, Z. Phys. A **56**, 330 (1921).
[2] S. Xu *et al.*, Discovery of a Weyl fermion semimetal and topological Fermi arcs, Science **349**, 613 (2015).
[3] M. Xiao, W.-J. Chen, W.-Y. He, and C. T. Chan, Synthetic gauge flux and Weyl points in acoustic systems, Nat. Phys. **11**, 920 (2015).
[4] D. Z. Rocklin, B. G. G. Chen, M. Falk, V. Vitelli, and T. C. Lubensky, Mechanical Weyl Modes in Topological Maxwell Lattices, Phys. Rev. Lett. **116**, 135503 (2016).
[5] L. Lu, Z. Wang, D. Ye, L. Ran, L. Fu, J. D. Joannopoulos, and M. Soljačić, Experimental observation of Weyl points, Science **349**, 622 (2015).
[6] Q. Lin, M. Xiao, L. Yuan, and S. Fan, Photonic Weyl point in a two-dimensional resonator lattice with a synthetic frequency dimension, Nat. Commun. **7**, 13731 (2016).
[7] Q. Wang, M. Xiao, H. Liu, S. Zhu, and C. T. Chan, Optical Interface States Protected by Synthetic Weyl Points, Phys. Rev. X **7**, 031032 (2017).
[8] T. Zhang, Z. Song, A. Alexandradinata, H. Weng, C. Fang, L. Lu, and Z. Fang, Double-Weyl Phonons in Transition-Metal Monosilicides, Phys. Rev. Lett. **120**, 016401 (2018).
[9] W. J. Chen, M. Xiao, and C. T. Chan, Photonic crystals possessing multiple Weyl points and the experimental observation of robust surface states, Nat. Commun. **7**, 13038 (2016).
[10] F. Li, X. Huang, J. Lu, J. Ma, and Z. Liu, Weyl points and Fermi arcs in a chiral phononic crystal, Nat. Phys. **14**, 30 (2018).
[11] H. Ge, X. Ni, Y. Tian, S. K. Gupta, M. H. Lu, X. Lin, W. D. Huang, C. T. Chan, and Y. F. Chen, Experimental Observation of Acoustic Weyl Points and Topological Surface States, Phys. Rev. Applied **10**, 014017 (2018).
[12] X. Zhang, M. Xiao, Y. Cheng, M. H. Lu, and J. Christensen, Topological sound, Commun. Phys. **1**, 97 (2018).
[13] Y. Qi *et al.*, Superconductivity in Weyl semimetal candidate $MoTe_2$, Nat. Commun. **7**, 11038 (2016).
[14] G. Bednik, A. A. Zyuzin, and A. A. Burkov, Superconductivity in Weyl metals, Phys. Rev. B **92**, 035153 (2015).
[15] V. Peri, M. Serra-Garcia, R. Ilan, and S. D. Huber, Axial-field-induced chiral channels in an acoustic Weyl system, Nat. Phys. **15**, 357 (2019).
[16] H. He, C. Qiu, L. Ye, X. Cai, X. Fan, M. Ke, F. Zhang, and Z. Liu, Topological negative refraction of surface acoustic waves in a Weyl phononic crystal, Nature (London) **560**, 61 (2018).
[17] T. Ozawa *et al.*, Topological photonics, Rev. Mod. Phys. **91**, 015006 (2019).
[18] T. Chen, J. R. Jiao, H. Q. Dai, and D. J. Yu, Acoustic Weyl points in a square lattice, Phys. Rev. B **98**, 214110 (2018).
[19] T. Liu *et al.*, Acoustic semimetal with Weyl points and surface states, arXiv:1803.04284.
[20] A. A. Soluyanov, D. Gresch, Z. Wang, Q. Wu, M. Troyer, X. Dai, and B. A. Bernevig, Type-II Weyl semimetals, Nature (London) **527**, 495 (2015).
[21] Y. Wang *et al.*, Gate-tunable negative longitudinal magnetoresistance in the predicted type-II Weyl semimetal WTe_2, Nat. Commun. **7**, 13142 (2016).
[22] M. Milićević *et al.*, Type-III and Tilted Dirac Cones Emerging from Flat Bands in Photonic Orbital Graphene, Phys. Rev. X **9**, 031010 (2019).
[23] Y. Xu, F. Zhang, and C. Zhang, Structured Weyl Points in Spin-Orbit Coupled Fermionic Superfluids, Phys. Rev. Lett. **115**, 265304 (2015).
[24] Z. Yu, Y. Yugui, and A. Y. Shengyuan, Predicted Unusual Magnetoresponse in Type-II Weyl Semimetals, Phys. Rev. Lett. **117**, 077202 (2016).
[25] Y. Xu and L. M. Duan, Type-II Weyl points in three-dimensional cold-atom optical lattices, Phys. Rev. A **94**, 053619 (2016).
[26] Z. Yang and B. Zhang, Acoustic Type-II Weyl Nodes from Stacking Dimerized Chains, Phys. Rev. Lett. **117**, 224301 (2016).
[27] B. Xie, H. Liu, H. Cheng, Z. Liu, S. Chen, and J. Tian, Experimental Realization of Type-II Weyl Points and Fermi Arcs in Phononic Crystal, Phys. Rev. Lett. **122**, 104302 (2019).
[28] G. Sharma, P. Goswami, and S. Tewari, Chiral anomaly and longitudinal magnetotransport in type-II Weyl semimetals, Phys. Rev. B **96**, 045112 (2017).
[29] A. A. Zyuzin and R. P. Tiwari, Intrinsic anomalous Hall effect in type-II Weyl semimetals, JETP Lett. **103**, 717 (2016).
[30] I. Liberal and N. Engheta, Near-zero refractive index photonics, Nat. Photonics **11**, 149 (2017).

[31] M. Silveirinha and N. Engheta, Design of matched zero-index metamaterials using nonmagnetic inclusions in epsilon-near-zero media, Phys. Rev. B **75**, 075119 (2007).
[32] X. Huang Y. Lai, Z. Hong Hang, H. Zheng, and C. T. Chan, Dirac cones induced by accidental degeneracy in photonic crystals and zero-refractive-index materials, Nat. Mater. **10**, 582 (2011).
[33] R. Fleury and A. Alù, Extraordinary Sound Transmission through Density-Near-Zero Ultranarrow Channels, Phys. Rev. Lett. **111**, 055501 (2013).
[34] See Supplemental Material at http://link.aps.org/supplemental/10.1103/PhysRevLett.125.054301 for the topological description of the proposed type-III Weyl semimetal, geometrical descriptions, numerical methods, experimental methods, anomalous tunneling based on type-III semimetals, effect of losses on the supercoupling effect, Fermi surface of the proposed semimetal, zero-index Weyl semimetals based on electromagnetic waves, observation of type-I and type-II acoustic Weyl semimetals in the proposed sonic crystal, and analogy between type-III Dirac semimetals and topological cut planes of type-III Weyl semimetals, which includes Refs. [23,35–39].
[35] T. Morimoto and A. Furusaki, Weyl and Dirac semimetals with $\mathbb{Z}_2$ topological charge, Phys. Rev. B **89**, 235127 (2014).
[36] D. R. Smith, D. C. Vier, T. Koschny, and C. M. Soukoulis, Electromagnetic parameter retrieval from inhomogeneous metamaterials, Phys. Rev. E **71**, 036617 (2005).
[37] M. R. Stinson, The propagation of plane sound waves in narrow and wide circular tubes, and generalization to uniform tubes of arbitrary cross-sectional shape, J. Acoust. Soc. Am. **89**, 550 (1991).
[38] N. Jiménez, V. Romero-García, V. Pagneux, and J.-P. Groby, Quasiperfect absorption by subwavelength acoustic panels in transmission using accumulation of resonances due to slow sound, Phys. Rev. B **95**, 014205 (2017).
[39] G. Theocharis, O. Richoux, V. Romero García, A. Merkel, and V. Tournat, Limits of slow sound propagation and transparency in lossy, locally resonant periodic structures, New J. Phys. **16**, 093017 (2014).
[40] Y. Li, W. Ying, and M. Jun, Double Dirac cones in phononic crystals, Appl. Phys. Lett. **105**, 014107 (2014).
[41] T. Ozawa and H. M. Price, Topological quantum matter in synthetic dimensions, Nat. Rev. Phys. **1** (2019).
[42] E. Lustig, S. Weimann, Y. Plotnik, Y. Lumer, M. A. Bandres, A. Szameit, and M. Segev, Photonic topological insulator in synthetic dimensions, Nature (London) **567**, 356 (2019).
[43] X. Fan, C. Qiu, Y. Shen, H. He, M. Xiao, M. Ke, and Z. Liu, Probing Weyl Physics with One-Dimensional Sonic Crystals, Phys. Rev. Lett. **122**, 136802 (2019).
[44] L. Yuan, Q. Lin, M. Xiao, and S. Fan, Synthetic dimension in photonics, Optica **5**, 1396 (2018).
[45] C. W. Hsu, B. Zhen, A. D. Stone, J. D. Joannopoulos, and M. Soljačić, Bound states in the continuum, Nat. Rev. Mater. **1**, 16048 (2016).
[46] L. Carletti, K. Koshelev, C. De Angelis, and Y. Kivshar, Giant Nonlinear Response at the Nanoscale Driven by Bound States in the Continuum, Phys. Rev. Lett. **121**, 033903 (2018).
[47] M. I. Molina, A. E. Miroshnichenko, and Y. S. Kivshar. Surface Bound States in the Continuum, Phys. Rev. Lett. **108**, 070401 (2012).
[48] F. Zangeneh-Nejad and R. Fleury, Topological Fano Resonances, Phys. Rev. Lett. **122**, 014301 (2019).
[49] Y. X. Xiao, G. Ma, Z. Q. Zhang, and C. T. Chan, Topological Subspace-Induced Bound State in the Continuum, Phys. Rev. Lett. **118**, 166803 (2017).